

Supplementary Materials for  
**Long-lasting, deep effect of Saturn's giant storms**

Cheng Li *et al.*

Corresponding author: Cheng Li, chengcli@umich.edu

*Sci. Adv.* **9**, eadg9419 (2023)  
DOI: 10.1126/sciadv.adg9419

**This PDF file includes:**

Sections A to C  
Figs. S1 to S8  
Table S1  
References

# Long-lasting, deep effect of Saturn's Giant Storms

## Supplementary Material

### A Deep ammonia abundance

Briggs et al. (1989) determined Saturn's deep NH<sub>3</sub> abundance to be 3× solar N ( $\sim 390$  ppm) by fitting a thermo-chemical equilibrium model to the data (21, 22). With an H<sub>2</sub>S abundance of  $\sim 10\times$  solar, they effectively decreased the ammonia abundance in the upper atmosphere to a near-solar value ( $\sim 120$  ppm). In contrast, we use a fitted constant value 200 ppm for the NH<sub>3</sub> abundance throughout the atmosphere, from the deep atmosphere up to the cloud condensation level; at and above this level NH<sub>3</sub> follows the saturated vapor curve. We refer to this value (200 ppm) as the deep ammonia abundance. Note that the acquired VLA data lose sensitivity to pressure levels greater than 20 bars. So the deep ammonia abundance refers to the concentration of ammonia above the water cloud level, which is approximately at 20 bars given  $\sim 10\times$  solar oxygen abundance. There is no noticeable difference in disk-averaged spectra based upon an ammonia abundance profile as used by Briggs et al. (1989) (22) or us. In the following, we compute a grid of disk models using different deep ammonia abundances to show the goodness-of-fit to the disk-averaged brightness temperature.

Fig. S1 shows the  $\chi^2$  fitting of six radio bands as a function of the deep ammonia abundance. As seen in the figure, the Q, K and U bands are not sensitive to the choice of the deep ammonia abundance because their weighting functions are in the ammonia cloud layer. The  $\chi^2$  values of the U-band data are slightly greater than 1, signifying a small departure from a homogenous and adiabatic atmosphere near a few bars. X-band starts to show some sensitivity such that  $\chi^2$  decreases with increasing deep ammonia abundance. The  $\chi^2$  is less than one when the deep ammonia abundance is greater than 150 ppm. The fittings to the C and S bands are the most illuminating. Their  $\chi^2$  values reach minimum (less than 1) when the deep ammonia

abundance is near 200 ppm. We have not attempted to get a formal uncertainty because the calibration uncertainty is imprecise and the disk-averaged model only serves as a balance model for the differential fitting, which does not affect the accuracy of the differential inversion. So we adopt 200 ppm as the deep ammonia abundance for the baseline model. Observations of Saturn at longer wavelengths or an entry probe are needed to characterize both this number and its uncertainty more proficiently (50).

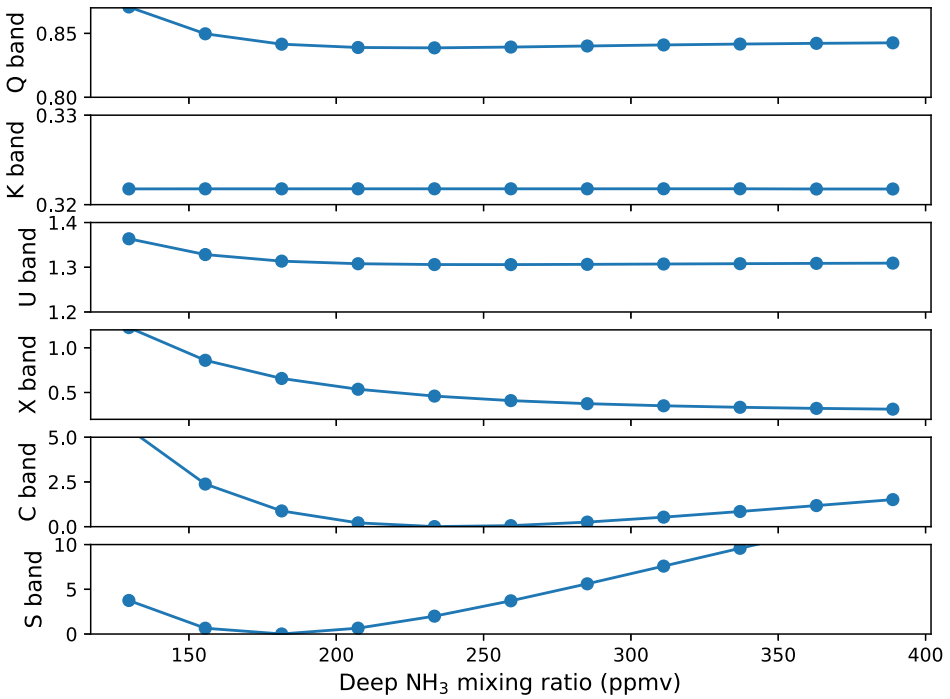


Fig. S 1  $\chi^2$  values of the fitting to the disk-averaged brightness temperatures as a grid of deep ammonia concentration. The radio bands are ordered from top to bottom with increasing wavelength. The horizontal axis, indicating the deep ammonia concentration, is common for all bands.

## B Synthetic study of a triangular signal

In the previous section, we described a way to deconvolve the convolved brightness temperature signal. In this section, we demonstrate the effectiveness of the deconvolution algorithm based on

a known truth, an isolated triangular signal. We first convolve the signal with a Gaussian beam and then deconvolve it using the deconvolution algorithm. We check whether our algorithm can successfully recover the original triangular signal. The isolated triangular signal is described as,  $\phi(x; d)$ , where

$$\phi(x; d) = \begin{cases} |x|/d, & \text{if } |x| < d \\ 0, & \text{otherwise} \end{cases} \quad (26)$$

is the general triangular function at  $x = 0$ . We choose to test a triangular signal because it is single-peaked, has a finite width, and is the basic element for the linear segmentation of a continuous signal. The convolution of a triangular function with a Gaussian beam has an analytical form, which is:

$$\begin{aligned} A(x; d, s) &= \int_{-\infty}^{+\infty} \phi(y; d) G(x - y; s) dy \\ &= \left( \exp\left(-\frac{(d+x)^2}{2\sigma^2}\right) + \exp\left(-\frac{(d-x)^2}{2\sigma^2}\right) - 2 \exp\left(-\frac{x^2}{2\sigma^2}\right) \right) \frac{\sigma}{\sqrt{2\pi}d} \\ &\quad + \left( (d+x)\text{Erf}\left(\frac{d+x}{\sqrt{2}\sigma}\right) + (d-x)\text{Erf}\left(\frac{d-x}{\sqrt{2}\sigma}\right) - 2x\text{Erf}\left(\frac{x}{\sqrt{2}\sigma}\right) \right) \frac{1}{2d}. \end{aligned} \quad (27)$$

There are three controlling parameters: the FWHM of the Gaussian beam ( $s = 2\sqrt{2 \ln 2}\sigma$ ), the FWHM of the triangular signal ( $d$ ), and the spatial resolution of the sampling ( $\delta x$ ). We fix  $s = 0.2355$  ( $\sigma = 0.1$ ) and vary  $d$  and  $\delta x$ . If the width of the signal is much larger than the width of the beam, one would expect that the signal can be fully recovered after deconvolution. This synthetic study is used to determine the ideal combination of sampling and signal width for the inversion.

Figs. S3 and S4 show a limiting case in which the width of the signal (orange patch,  $d = 0.2$ ) is slightly smaller than the width of beam (blue patch,  $s = 0.2355$ ). In Fig. S3, the spatial resolution of the sampling is  $\delta x = 0.1$ , which is about half of the FWHM of the beam. The result shows that the deconvolved signal (red line) is almost identical to the original signal (orange line). The deconvolution algorithm is also robust to white noise addition. The uncertainty of

the deconvolved signal with 10% white noise is indicated by the error ticks in the figure. Increasing the sampling rate (Fig. S4) usually does not lead to a better recovery because that also increases the degrees of freedom, i.e. the number of frequencies, as well. In fact, increasing the spatial information results in less information than what is needed to fully determine the spectral amplitudes at the high frequencies. Regularizing the solution using equation (11) damps out high-frequency modes and is essential to obtain a converged solution for a fine-resolution sampling. However, if the sampling solution is low, the shape of the source function may not be adequately sampled. Comparing Fig. S3 and Fig. S4 tells that one can use one-quarter of the width of the signal as the spatial sampling resolution to approximately recover the original signal. This improves the spatial resolution of the mapping.

Inspecting the spectral domain (bottom panels of Fig. S3 and S4) illuminates how the deconvolution is performed. Blue symbols show the spectra of beam-convolved observation with circles for the real part and crosses for the imaginary part. Red symbols show the spectra of the deconvolved signal, which are larger in magnitude than the blue symbols at high frequencies, showing that deconvolution amplifies the magnitude of the high-frequency modes. Without regularization, the amplification of noise at high-frequencies leads to instability of the deconvolution.

Figs. S5 and S6 test the situation in which the width of the signal is about half of the width of the beam. We also test two resolutions,  $\delta x = 0.1$  and  $\delta x = 0.05$  respectively. Similar to the previous studies, 10% white noise is introduced in the synthetic deconvolution study. We see small amplitude spurious oscillations next to the peak signal. Increasing the spatial sampling resolution (Fig. S6) does not eliminate the oscillations but rather acts as an interpolated result from a low-resolution solution. These exercises demonstrate that, for a given beam width, one can fully recover the signal with a similar width using 1/4 of the beam width as a spatial sampling resolution. This is the resolution we have used for the deconvolution of all radio band

data.

## C Inversion prior parameters and discussion

We have applied a prior standard deviation of 125 ppm for the ammonia concentration anomaly at every level. If fitting the data requires less than 125 ppm ammonia anomaly, the prior constraint does not have an effect. If more than 125 ppm ammonia anomaly is needed, the inversion algorithm would seek a balance between the goodness-of-fit to the data and satisfying the prior constraint, which means that magnitude of the fitted ammonia anomaly would be reduced (regularized) as the cost of sacrificing the goodness-of-fit to the data. For example, our inversion algorithm does not allow a zero ammonia abundance due to the prior constraint, but it generally allows ammonia to vary between  $50 \sim 350$  ppm. If the observed brightness temperature is too high or too low given the prescribed level of ammonia variability, the fitted ammonia anomaly would stay within the prescribed range regardless of the data. The potential mismatch between the data and model is not caused by the measurement accuracy but is due to a simplified representation of a complex atmosphere of infinite degrees of freedom, such as ignoring the temperature variability, dividing a continuous atmosphere into a few discrete levels, truncating the atmosphere at a finite depth, etc.

From the ammonia anomaly map (Fig. 5), we find that the prior constraint is generally satisfied for storms other than the most recent 2010 storm. This agrees with the prior study reporting that the atmosphere is devoid of ammonia vapor possibly down to 5 bars after the 2010 storm (12). Our prior constraint does not allow such an extreme condition to occur, but the ammonia anomaly map shows the largest ammonia variability exceeding the prescribed range of ammonia variability. Fig. S8 shows the comparison between the observed brightness temperature anomalies and the fitted ones based on the ammonia anomaly map in Fig. 5. We have obtained a good fit for the S and C band brightness temperature anomalies. General features

exhibited in X and U bands are captured, with the largest one being the positive brightness temperature anomaly at 44 °N. This anomaly exists in X, U, K, and Q-bands and is captured by the fits to these four bands. From the fits, the dip in brightness temperature at 43 °N exists in both U and X-bands. However, we only see a dip in the brightness temperature in the U-band data. There can be two possibilities. First, the latitude span of the gap (43 °N) is right at the spatial resolution of the U-band data but smaller than the spatial resolution of the X-band data. Second, the gap occupies an extremely small vertical layer (less than one bar pressure) that is only sensed by the U-band weighting function but not the X-band. Given that the weighting functions of the U-band and X-band are close (Fig. 1), we deem this possibility unlikely. The poorest fitting occurs at the K-band (still within a few K differences), whose weighting function is in the ammonia cloud. Therefore, the K-band data would be dominated by temperature variations rather than ammonia vapor. However, the major findings and conclusions of this work are not sensitive to the temperature or ammonia concentration inferred at the K-band because we drew our conclusion based on the ammonia anomalies between 2 ∼ 20 bars.

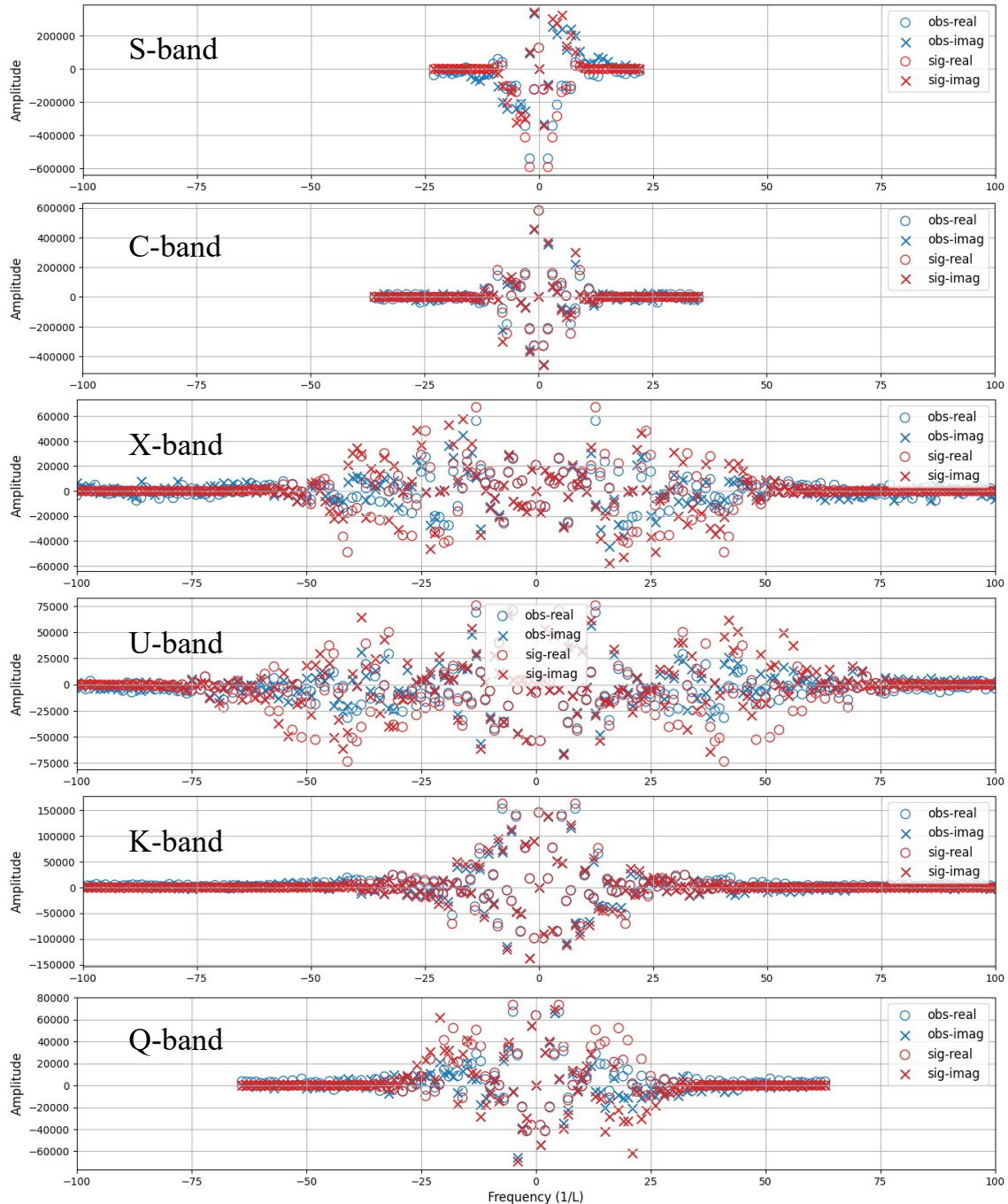


Fig. S 2 Spectral domain of the brightness temperatures at each band. (Blue) Fourier amplitudes of the observed (i.e., beam-convolved) brightness temperature; (red) Fourier amplitudes of the pointwise brightness temperature. The real part is displayed in circles and the imaginary part is in crosses.  $L$  refers to the diameter of Saturn's disk.

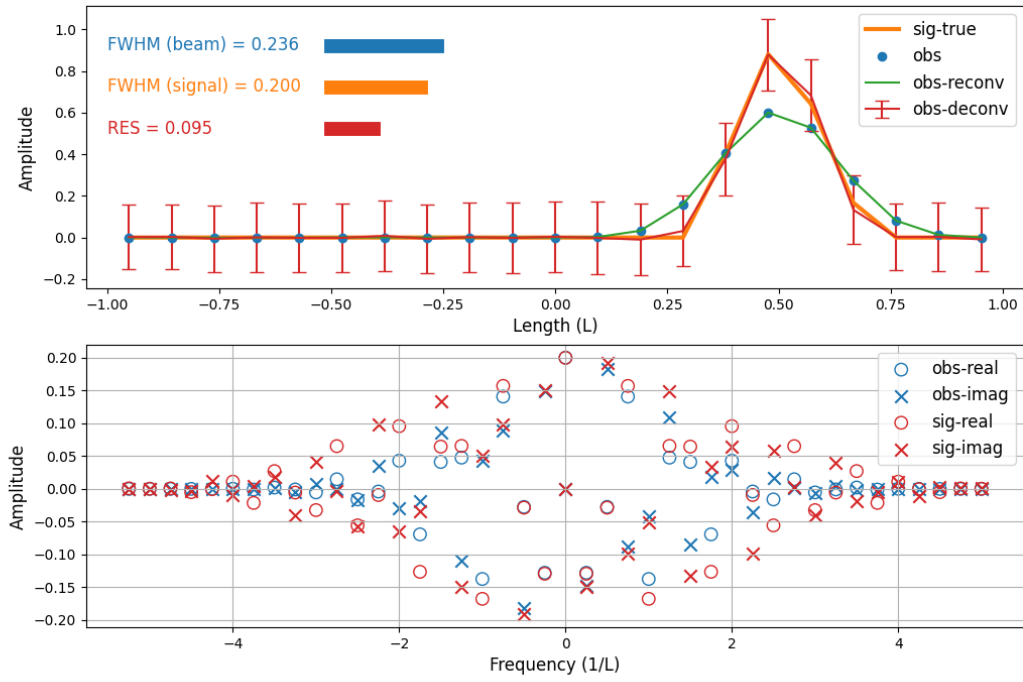


Fig. S 3 Top panel: Pointwise signal (orange line) and convolved observation (blue dots) in the physical domain. Red line with error ticks is the deconvolved signal. Green line shows the reconvolved observation using the deconvolved signal. Bottom panel: Circles show the real part of the Fourier amplitude in the spectral domain. Crosses show the imaginary part of the Fourier amplitude in the spectral domain. Blue colors are for the convolved observation and red colors are for the deconvolved signal. The Fourier coefficients are normalized such that the amplitude of the zero frequency mode equals the integral of the signal over the physical domain. The FWHMs of the Gaussian beam and the signals and the resolution of the sampling are printed and illustrated in the top panel.

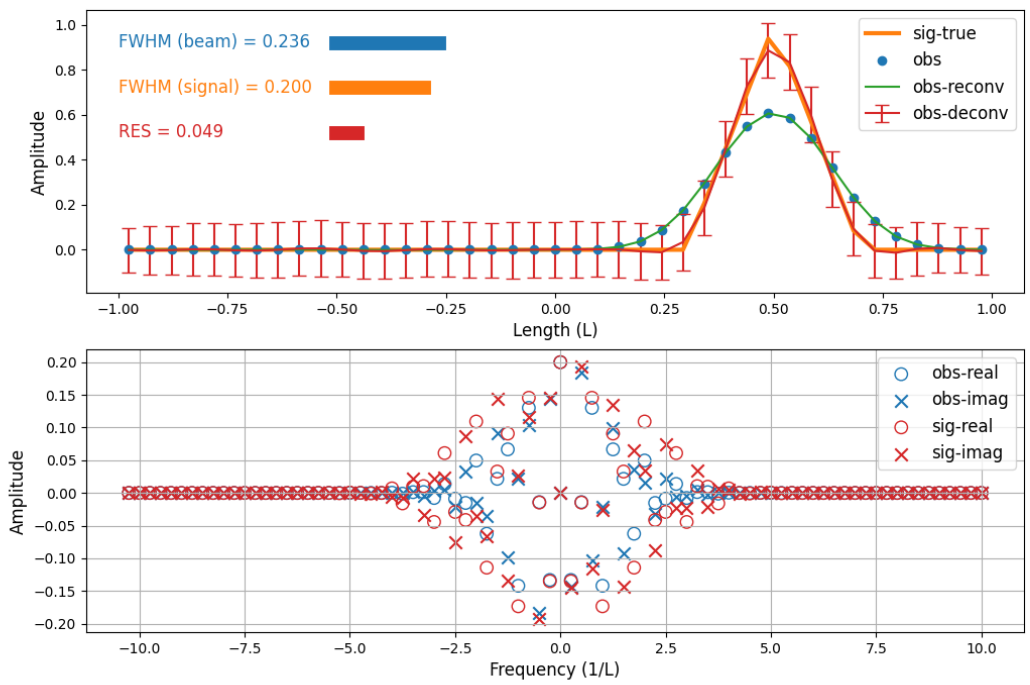


Fig. S 4 Similar to Fig. S3 but the sampling resolution is doubled.

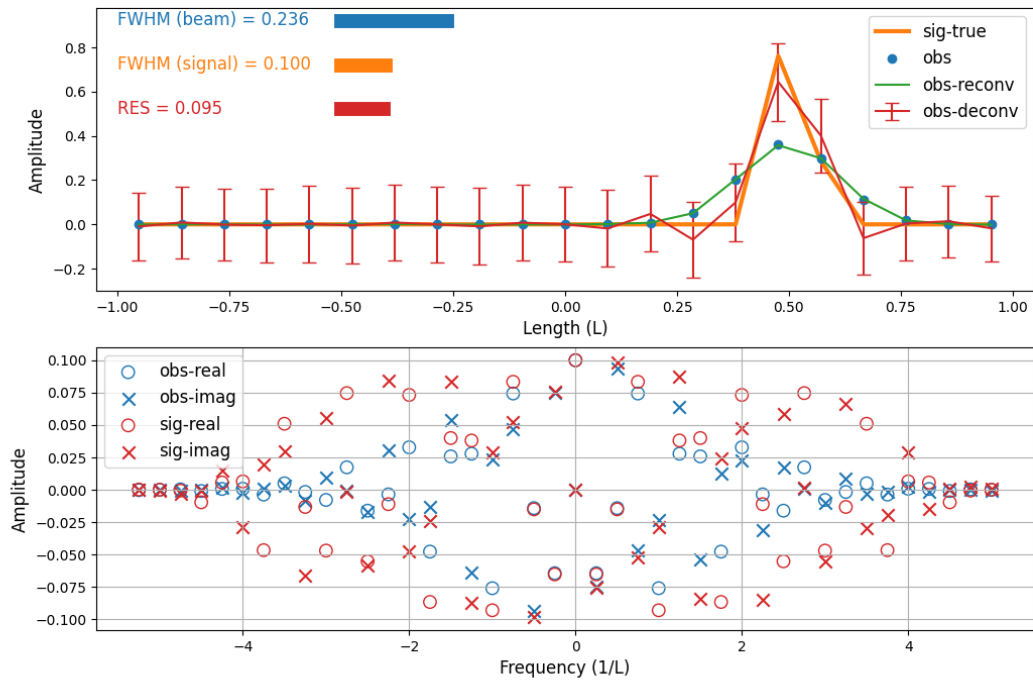


Fig. S 5 Similar to Fig. S3 but the width of the signal is halved.

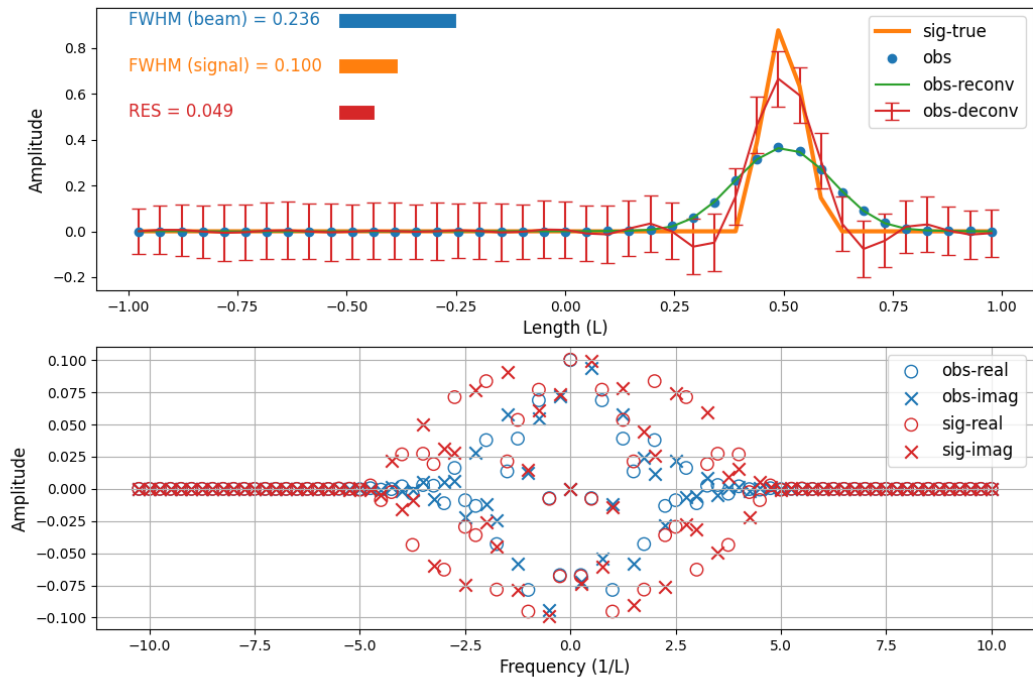


Fig. S 6 Similar to Fig. S3 but with half-width signal and double-resolution sampling.

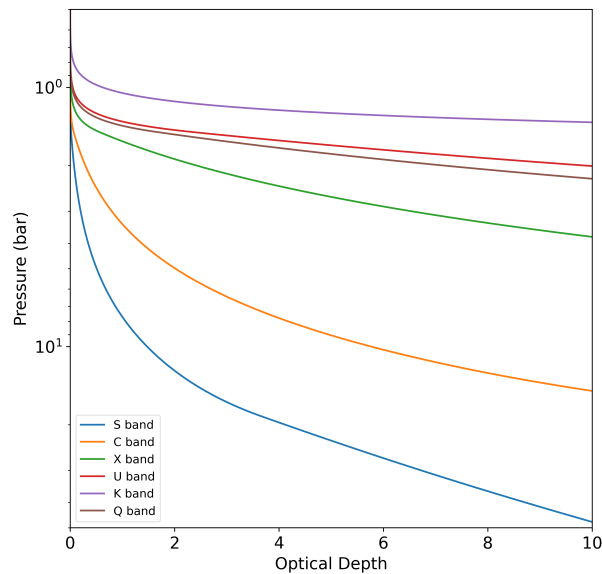


Fig. S 7 Optical depth as a function of pressure for six radio bands.

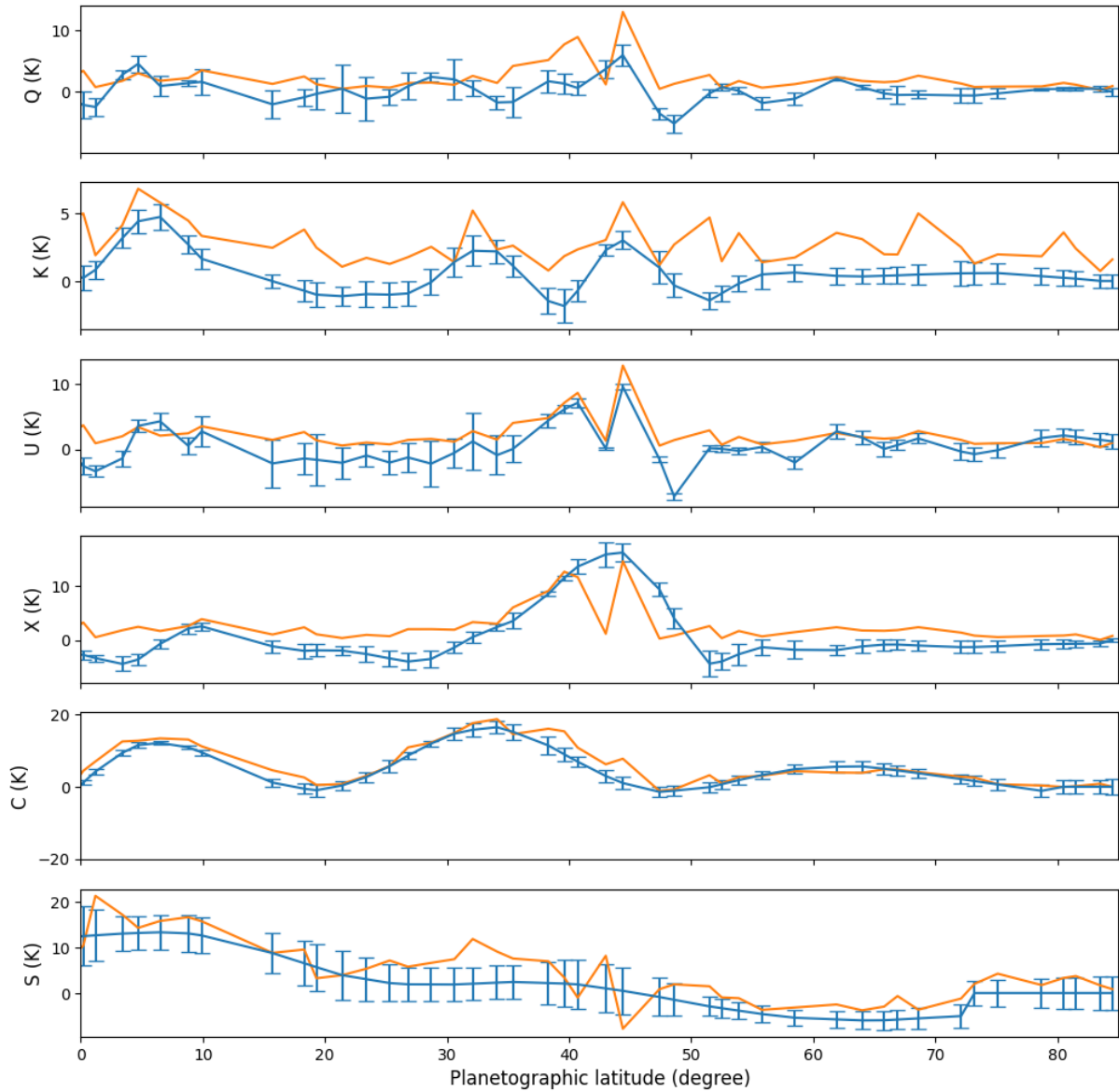


Fig. S 8 Blue lines with error ticks: observed brightness temperature anomalies of each band. Orange lines: fitted brightness temperature anomaly based on the ammonia anomaly reported in Fig. 5.

**Table S1.** Disk-averaged brightness temperature of Saturn (K)

Band	Frequ. $\nu$ (GHz)	$\Delta\nu$ (GHz)	Mean wavelength (cm)	Brightness $T_0$	Brightness $T_1$	$T_{cmb}$	Brightness $T_b$
S band	2.123	0.25	14.130	203.50	37.700	2.67	$231.3 \pm 7$
C band	4.100	0.25	7.317	168.50	16.850	2.63	$182.4 \pm 5.5$
X band	8.470	1.0	3.540	145.605	15.205	2.53	$158.3 \pm 4.7$
	9.510	1.0	3.150	143.545	13.150	2.50	$154.8 \pm 4.6$
	10.500	1.0	2.860	142.085	12.265	2.48	$152.7 \pm 4.5$
	11.300	1.0	2.650	139.985	12.175	2.46	$150.6 \pm 4.5$
U band	12.490	1.0	2.400	138.555	9.005	2.44	$147.0 \pm 4.4$
	13.490	1.0	2.220	135.880	10.475	2.41	$145.3 \pm 4.4$
	14.490	1.0	2.070	136.065	10.900	2.39	$145.7 \pm 4.4$
	15.512	1.0	1.930	136.340	11.010	2.37	$146.1 \pm 4.4$
	16.490	1.0	1.820	132.405	7.370	2.35	$139.7 \pm 4.2$
K band	20.000	4.0	1.500	126.885	11.850	2.27	$137.1 \pm 6.9$
	23.980	4.0	1.250	121.424	14.563	2.19	$133.3 \pm 6.7$
Q band	43.700	7.8	0.686	132.489	14.638	1.81	$144.1 \pm 7.2$

NOTE— $T_b = T_0 + T_1 \langle \mu_p \rangle + T_{cmb}$ , with  $\langle \mu_p \rangle = 0.667$ , and  $T_{cmb}$  the cosmic background radiation.

## REFERENCES AND NOTES

1. A. Sanchez-Lavega, E. Battaner, The nature of Saturn's atmospheric great white spots. *Astron. Astrophys.* **185**, 315–326 (1987).
2. A. Sanchez-Lavega, Saturn's great white spots *J. Nonlinear Sci.* **4**, 341–353 (1994).
3. K. M. Sayanagi, U. A. Dyudina, S. P. Ewald, G. Fischer, A. P. Ingersoll, W. S. Kurth, G. D. Muro, C. C. Porco, R. A. West, Dynamics of Saturn's great storm of 2010–2011 from cassini iss and rpws. *Icarus* **223**, 460–478 (2013).
4. A. Sánchez-Lavega, T. del Río-Gaztelurrutia, R. Hueso, J. M. Gómez-Forrellad, J. F. Sanz-Requena, J. Legarreta, E. García-Melendo, F. Colas, J. Lecacheux, L. N. Fletcher, D. Barrado-Navascués, D. Parker, The International Outer Planet Watch (IOPW) Team, Deep winds beneath Saturn's upper clouds from a seasonal long-lived planetary-scale storm. *Nature* **475**, 71–74 (2011).
5. G. Fischer, W. Kurth, D. Gurnett, P. Zarka, U. Dyudina, A. Ingersoll, S. Ewald, C. Porco, A. Wesley, C. Go, M. Delcroix, A giant thunderstorm on Saturn. *Nature* **475**, 75–77 (2011).
6. C. Li, A. P. Ingersoll, Moist convection in hydrogen atmospheres and the frequency of Saturn's giant storms. *Nat. Geosci.* **8**, 398–403 (2015).
7. L. N. Fletcher, B. Hesman, R. Achterberg, P. Irwin, G. Bjoraker, N. Gorius, J. Hurley, J. Sinclair, G. Orton, J. Legarreta, E. García-Melendo, A. Sánchez-Lavega, P. L. Read, A. A. Simon-Miller, F. M. Flasar, The origin and evolution of Saturn's 2011–2012 stratospheric vortex. *Icarus* **221**, 560–586 (2012).
8. L. N. Fletcher, S. Guerlet, G. S. Orton, R. G. Cosentino, T. Fouchet, P. G. Irwin, L. Li, F. M. Flasar, N. Gorius, R. Morales-Juberías, Disruption of Saturn's quasi-periodic equatorial oscillation by the great northern storm *Nat. Astron.* **1**, 765–770 (2017).
9. B. Hesman, G. Bjoraker, P. Sada, R. Achterberg, D. Jennings, P. Romani, A. Lunsford, L. Fletcher, R. Boyle, A. Simon-Miller, C. A. Nixon, P. G. J. Irwin, Elusive ethylene detected in Saturn's northern storm region. *Astrophys. J.* **760**, 24 (2012).
10. J. I. Moses, E. S. Armstrong, L. N. Fletcher, A. J. Friedson, P. G. Irwin, J. A. Sinclair, B. E. Hesman, Evolution of stratospheric chemistry in the Saturn storm beacon region. *Icarus* **261**, 149–168 (2015).
11. M. Janssen, A. Ingersoll, M. Allison, S. Gulkis, A. Laraia, K. Baines, S. Edgington, Y. Anderson, K. Kelleher, F. Oyafuso, Saturn's thermal emission at 2.2-cm wavelength as imaged by the cassini radar radiometer. *Icarus* **226**, 522–535 (2013).

12. A. Laraia, A. Ingersoll, M. A. Janssen, S. Gulkis, F. Oyafuso, M. Allison, Analysis of Saturn’s thermal emission at 2.2-cm wavelength: Spatial distribution of ammonia vapor. *Icarus* **226**, 641–654 (2013).
13. A. P. Showman, I. de Pater, Dynamical implications of Jupiter’s tropospheric ammonia abundance. *Icarus* **174**, 192–204 (2005).
14. T. Guillot, D. J. Stevenson, S. K. Atreya, S. J. Bolton, H. N. Becker, Storms and the depletion of ammonia in Jupiter: I. microphysics of “mushballs”. *J. Geophys. Res. Planets* **125**, e2020JE006403 (2020).
15. T. Guillot, C. Li, S. J. Bolton, S. T. Brown, A. P. Ingersoll, M. A. Janssen, S. M. Levin, J. I. Lunine, G. S. Orton, P. G. Steffes, D. J. Stevenson, Storms and the depletion of ammonia in Jupiter: II. Explaining the juno observations. *J. Geophys. Res. Planets* **125**, e2020JE006404 (2020).
16. S. Weidenschilling, J. Lewis, Atmospheric and cloud structures of the jovian planets. *Icarus* **20**, 465–476 (1973).
17. L. Li, B. J. Conrath, P. J. Gierasch, R. K. Achterberg, C. A. Nixon, A. A. Simon-Miller, F. M. Flasar, D. Banfield, K. H. Baines, R. A. West, A. P. Ingersoll, A. R. Vasavada, A. D. del Genio, C. C. Porco, A. Mamoutkine, M. E. Segura, G. L. Bjoraker, G. S. Orton, L. N. Fletcher, P. G. J. Irwin, P. L. Read, Saturn’s emitted power. *J. Geophys. Res. Planets* **115**, E11002 (2010).
18. Z. Zhang, A. Hayes, I. de Pater, D. Dunn, M. Janssen, P. Nicholson, J. Cuzzi, B. Butler, R. Sault, S. Chatterjee, VLA multi-wavelength microwave observations of Saturn’s C and B rings. *Icarus* **317**, 518–548 (2019).
19. M. Wright, R. Sault, Mapping cygnus a at 3 millimeter wavelength with the miriad system. *Astrophys. J.* **402**, 546–549 (1993).
20. G. F. Lindal, The atmosphere of Neptune: An analysis of radio occultation data acquired with Voyager 2. *Astron. J.* **103**, 967–982 (1992).
21. M. Asplund, N. Grevesse, A. J. Sauval, P. Scott, The chemical composition of the sun. *Annu. Rev. Astron. Astrophys.* **47**, 481–522 (2009).
22. F. H. Briggs, P. D. Sackett, Radio observations of Saturn as a probe of its atmosphere and cloud structure. *Icarus* **80**, 77–103 (1989).
23. I. de Pater, E. M. Molter, C. M. Moeckel, A review of radio observations of the giant planets: Probing the composition, structure, and dynamics of their deep atmospheres. *Remote Sens.* **15**, 1313 (2023).
24. C. Li, A. Ingersoll, M. Janssen, S. Levin, S. Bolton, V. Adumitroaie, M. Allison, J. Arballo, A. Bellotti, S. Brown, S. Ewald, L. Jewell, S. Misra, G. Orton, F. Oyafuso, P. Steffes, R. Williamson, The

- distribution of ammonia on Jupiter from a preliminary inversion of juno microwave radiometer data. *Geophys. Res. Lett.* **44**, 5317–5325 (2017).
25. I. de Pater, D. Dunn, P. Romani, K. Zahnle, Reconciling Galileo probe data and ground-based radio observations of ammonia on Jupiter. *Icarus* **149**, 66–78 (2001).
26. C. Moeckel, I. de Pater, D. DeBoer, Ammonia abundance derived from juno mwr and vla observations of Jupiter. *Planet. Sci. J.* **4**, 25 (2023).
27. L. Fletcher, P. Irwin, G. Orton, N. Teanby, R. Achterberg, G. Bjoraker, P. Read, A. Simon-Miller, C. Howett, R. De Kok, N. Bowles, S. B. Calcutt, B. Hesman, F. M. Flasar, Temperature and composition of Saturn’s polar hot spots and hexagon. *Science* **319**, 79–81 (2008).
28. R. Perley, K. Meisenheimer, High-fidelity VLA imaging of the radio structure of 3C273. *Astron. Astrophys.* **601**, A35 (2017).
29. L. Li, X. Jiang, H. J. Trammell, Y. Pan, J. Hernandez, B. J. Conrath, P. J. Gierasch, R. K. Achterberg, C. A. Nixon, F. M. Flasar, S. Perez-Hoyos, R. A. West, K. H. Baines, B. Knowles, Saturn’s giant storm and global radiant energy. *Geophys. Res. Lett.* **42**, 2144–2148 (2015).
30. L. Fletcher, P. Irwin, N. Teanby, G. Orton, P. Parrish, R. de Kok, C. Howett, S. Calcutt, N. Bowles, F. Taylor, Characterising Saturn’s vertical temperature structure from Cassini/CIRS. *Icarus* **189**, 457–478 (2007).
31. L. N. Fletcher, K. H. Baines, T. W. Momary, A. P. Showman, P. G. Irwin, G. S. Orton, M. Roos-Serote, C. Merlet, Saturn’s tropospheric composition and clouds from cassini/vims 4.6–5.1 $\mu$ m nightside spectroscopy. *Icarus* **214**, 510–533 (2011).
32. M. D. Desch, M. Kaiser, Voyager measurement of the rotation period of Saturn’s magnetic field. *Geophys. Res. Lett.* **8**, 253–256 (1981).
33. M. K. Dougherty, H. Cao, K. K. Khurana, G. J. Hunt, G. Provan, S. Kellock, M. E. Burton, T. A. Burk, E. J. Bunce, S. W. Cowley, M. G. Kivelson, C. T. Russell, D. J. Southwood, Saturn’s magnetic field revealed by the cassini grand finale. *Science* **362**, eaat5434 (2018).
34. P. Read, T. Dowling, G. Schubert, Saturn’s rotation period from its atmospheric planetary-wave configuration. *Nature* **460**, 608–610 (2009).
35. J. D. Anderson, G. Schubert, Saturn’s gravitational field, internal rotation, and interior structure. *Science* **317**, 1384–1387 (2007).
36. C. Mankovich, M. S. Marley, J. J. Fortney, N. Movshovitz, Cassini ring seismology as a probe of Saturn’s interior. I. Rigid rotation. *Astrophys J.* **871**, 1 (2019).

37. R. A. Perley, B. J. Butler, An accurate flux density scale from 1 to 50 ghz. *Astrophys. J. Suppl. Ser.* **204**, 19 (2013).
38. D. E. Dunn, L. A. Molnar, J. D. Fix, More microwave observations of Saturn: Modeling the ring with a monte carlo radiative transfer code. *Icarus* **160**, 132–160 (2002).
39. R. Brown, P. Hwang, *Introduction to Random Signals and Applied Kalman Filtering* (John Wiley & Sons Inc., 1992).
40. E. Sekko, G. Thomas, A. Boukrouche, A deconvolution technique using optimal wiener filtering and regularization. *Signal Process.* **72**, 23–32 (1999).
41. C. Li, T. Le, X. Zhang, Y. L. Yung, A high-performance atmospheric radiation package: With applications to the radiative energy budgets of giant planets. *J. Quant. Spectrosc. Radiat. Transf.* **217**, 353–362 (2018).
42. M. Klein, M. Janssen, S. Gulkis, E. Olsen, Saturn’s microwave spectrum: Implications for the atmosphere and the rings, in *Its The Saturn System* (NASA, 1978).
43. I. De Pater, J. R. Dickel, Multifrequency radio observations of Saturn at ring inclination angles between 5 and 26 degrees. *Icarus* **94**, 474–492 (1991).
44. F. van der Tak, I. de Pater, A. Silva, R. Millan, Time variability in the radio brightness distribution of Saturn. *Icarus* **142**, 125–147 (1999).
45. J. Weiland, N. Odegard, R. Hill, E. Wollack, G. Hinshaw, M. Greason, N. Jarosik, L. Page, C. Bennett, J. Dunkley, B. Gold, M. Halpern, A. Kogut, E. Komatsu, D. Larson, M. Limon, S. S. Meyer, M. R. Nolta, K. M. Smith, D. N. Spergel, G. S. Tucker, E. L. Wright, Seven-year Wilkinson microwave anisotropy probe (wmap\*) observations: Planets and celestial calibration sources. *Astrophys. J. Suppl. Ser.* **192**, 19 (2011).
46. Planck Collaboration, Y. Akrami, M. Ashdown, J. Aumont, C. Baccigalupi, M. Ballardini, A. J. Banday, R. B. Barreiro, N. Bartolo, S. Basak, K. Benabed, J.-P. Bernard, M. Bersanelli, P. Bielewicz, L. Bonavera, J. R. Bond, J. Borrill, F. R. Bouchet, F. Boulanger, M. Bucher, C. Burigana, R. C. Butler, E. Calabrese, J.-F. Cardoso, J. Carron, H. C. Chiang, L. P. L. Colombo, B. Comis, F. Couchot, A. Coulais, B. P. Crill, A. Curto, F. Cuttaia, P. de Bernardis, A. de Rosa, G. de Zotti, J. Delabrouille, E. Di Valentino, C. Dickinson, J. M. Diego, O. Doré, A. Ducout, X. Dupac, F. Elsner, T. A. Enßlin, H. K. Eriksen, E. Falgarone, Y. Fantaye, F. Finelli, M. Frailis, A. A. Fraisse, E. Franceschi, A. Frolov, S. Galeotta, S. Galli, K. Ganga, R. T. Génova-Santos, M. Gerbino, J. González-Nuevo, K. M. Górski, A. Gruppuso, J. E. Gudmundsson, F. K. Hansen, G. Helou, S. Henrot-Versillé, D. Herranz, E. Hivon, A. H.

- Jaffe, W. C. Jones, E. Keihänen, R. Keskitalo, K. Kiiveri, J. Kim, T. S. Kisner, N. Krachmalnicoff, M. Kunz, H. Kurki-Suonio, G. Lagache, J.-M. Lamarre, A. Lasenby, M. Lattanzi, C. R. Lawrence, M. Le Jeune, E. Lellouch, F. Levrier, M. Liguori, P. B. Lilje, V. Lindholm, M. López-Caniego, Y.-Z. Ma, J. F. Macías-Pérez, G. Maggio, D. Maino, N. Mandolesi, M. Maris, P. G. Martin, E. Martínez-González, S. Matarrese, N. Mauri, J. D. McEwen, A. Melchiorri, A. Mennella, M. Migliaccio, M.-A. Miville-Deschénes, D. Molinari, A. Moneti, L. Montier, R. Moreno, G. Morgante, P. Natoli, C. A. Oxborrow, D. Paoletti, B. Partridge, G. Patanchon, L. Patrizii, O. Perdereau, F. Piacentini, S. Plaszczynski, G. Polenta, J. P. Rachen, B. Racine, M. Reinecke, M. Remazeilles, A. Renzi, G. Rocha, E. Romelli, C. Rosset, G. Roudier, J. A. Rubiño-Martin, B. Ruiz-Granados, L. Salvati, M. Sandri, M. Savelainen, D. Scott, G. Sirri, L. D. Spencer, A.-S. Suur-Uski, J. A. Tauber, D. Tavagnacco, M. Tenti, L. Toffolatti, M. Tomasi, M. Tristram, T. Trombetti, J. Valiviita, F. Van Tent, P. Vielva, F. Villa, I. K. Wehus, A. Zacchei, Planck intermediate results: LII. Planet flux densities. *Astron. Astrophys.* **607**, A122 (2017).
47. M. Maris, E. Romelli, M. Tomasi, A. Gregorio, M. Sandri, S. Galeotta, D. Tavagnacco, M. Frailis, G. Maggio, A. Zacchei, Revised planet brightness temperatures using the Planck/LFI 2018 data release. *Astron. Astrophys.* **647**, A104 (2021).
48. I. de Pater, B. Butler, R. J. Sault, A. Moullet, C. Moeckel, J. Tollefson, K. de Kleer, M. Gurwell, S. Milam, in *Science with a Next Generation Very Large Array*, E. Murphy, Ed. (Astronomical Society of the Pacific, 2018), vol. 517 of Astronomical Society of the Pacific Conference Series, p. 49.
49. A. Sanchez-Lavega, F. Colas, J. Lecacheux, P. Laques, I. Miyazaki, D. Parker, The great white spot and disturbances in Saturn's equatorial atmosphere during 1990. *Nature* **353**, 397–401 (1991).
50. O. Mousis, L. Fletcher, J.-P. Lebreton, P. Wurz, T. Cavalié, A. Coustenis, R. Courtin, D. Gautier, R. Helled, P. G. J. Irwin, A. D. Morse, N. Nettelmann, B. Marty, P. Rousselot, O. Venot, D. H. Atkinson, J. H. Waite, K. R. Reh, A. Simon-Miller, S. Atreya, N. André, M. Blanc, I. A. Daglis, G. Fischer, W. D. Geppert, T. Guillot, M. M. Hedman, R. Hueso, E. Lellouch, J. I. Lunine, C. D. Murray, J. O'Donoghue, M. Rengel, A. Sanchez-Lavega, F.-X. Schmider, A. Spiga, T. Spilker, J.-M. Petit, M. S. Tiscareno, M. Ali-Dib, K. Altwegg, A. Bouquet, C. Briois, T. Fouchet, S. Guerlet, T. Kostiuk, D. Lebleu, R. Moreno, G. S. Orton, J. Poncy, Scientific rationale for Saturn's in situ exploration. *Planet. Space Sci.* **104**, 29–47 (2014).